RSM AND $\overline{v^2}$-*f* PREDICTIONS OF AN IMPINGING JET IN A CROSS FLOW ON A HEATED SURFACE AND ON A PEDESTAL

D. Rundström[1,2], B. Moshfegh[1,2] and A. Ooi[3]

[1]Division of Energy and Mechanical Engineering, Department of Technology and Built Environment, University of Gävle, Gävle, Sweden
[2]Department of Management and Engineering, Linköping University, Linköping, Sweden
[3] The University of Melbourne

Abstract

The objective of this study is to compare the performance of the $\overline{v^2}$-*f* and the Reynolds Stress Model (RSM) turbulence model with a two-layer wall treatment for the prediction of the mean velocity field, the turbulence characteristics and the heat transfer rate of the normal impinging jet and also impinging jet in a cross-flow configuration. The numerical predictions are validated against detailed experimental measurements, using PIV and a low-wavelength infrared imaging system, for the measurement of turbulent flow features and surface temperatures.

A linear pressure-strain model is used in the RSM. The turbulent heat fluxes are modeled by the eddy-diffusivity hypothesis with a constant value of the turbulent Prandtl number. The mesh is refined enough near the solid walls ($y^+ \approx 1$) to adequately resolve the boundary layers. The results show several complex flow-related phenomena that affect the cooling performance, such as stagnation point, separation region, curvature effects and re-circulating wake flows. These phenomena have to be accurately captured before a good prediction of the heat transfer rate can be attained. A comparison between the $\overline{v^2}$-*f* and RSM results in the stagnation region, in the other near-wall regions and in the free shear region will be presented in order to evaluate the performance of the two models.

1. Introduction

In the last two decades, there has been much research effort directed at understanding the flow and heat transfer from impinging jet flows. This is mainly due to the fact that the high heat transfer rates generated by turbulent impinging jet flows is present in modern design technologies used by industrial and engineering applications such as glass manufacturing, material processing and cooling of electronic chips. In electronic chip cooling, jet impingement is of interest due to the high heat transfer rates generated close to the impingement region. The method of cooling based on turbulent jet impingement is also widely used on the inner surfaces of vanes in modern gas turbines in order to prevent the metal temperature from overheating, see Brevet *et al.* [1]. Furthermore, jet impingement is also used as an effective method of drying film and textile; see Lee and Lee [13].

Many investigators have conducted experimental studies of different variations to the isolated normal round jet. For example,

Lee and Lee [13] and Lee and Baek [12] investigated the effect of the aspect ratio of elliptic (as opposed to circular) jets on the turbulent jet structure and heat transfer on the stagnation region of the plate. Choi *et al* [3] and Mesbah [17] have studied the heat transfer of the circular jet on concave surfaces. The effects of an isolated jet impinging on a circular pedestal have been investigated by Mesbah [17]. In order to investigate the confinement effects on the heat transfer of an impinging jet, Obot et al [18] and Garimella and Rice [7] have carried out experimental studies whereby a flat plate is placed in the vicinity of the jet exit to limit all fluid flow into a smaller region close to the plate.

The current trend in electronic devices shows a steady increase in the dissipated heat from electronic components. Forced channel flow is frequently used as a cooling technique, see Jonsson and Moshfegh [9] and Meinders and Hanjalić [15]. In combating the whole thermal load with forced channel flow, excessive flow rates will be required. In a typical electronic system, the printed circuit board (PCB) will contain one or a few high heat–dissipating components. One possible method to face this problem is to divide the channel flow in an impinging jet and a low-velocity cross-flow, see Rundström and Moshfegh [19]. The impinging jet is placed over the high heat-dissipating component and provides a local region with high cooling performance, especially at the stagnation point. The cross-flow is important to insure that well-distributed cooling performance is provided at the other parts of the PCBs, which require less cooling.

Two RANS-turbulence models, the $\overline{v^2}$-*f* model developed by Durbin [5] and a RSM with a two-layer model in the near-wall region were used by Rundström and Moshfegh [21] were used in an earlier validation study of the turbulent flow from an impinging jet in a cross-flow on a wall-mounted cube. The models showed similar results near the walls and the RSM predicted the flow and turbulence characteristics better than the $\overline{v^2}$-*f* model in the free shear regions (i.e. far from the walls). The accuracy of the heat transfer prediction from the RSM was investigated by Rundström and Moshfegh [20] and the main features were well predicted by the model in all regions except in the stagnation region of the impinging jet, where the model seems to overpredict the heat transfer rate. The accuracy of the predicted heat transfer rate from the $\overline{v^2}$-*f* model is investigated in the first part of this study.

2. COMPUTATIONAL SET-UP AND NUMERICAL SCHEME

2.1 Geometrical set-up and boundary conditions

The computational domain is a rectangular channel with a heated wall-mounted heated cube in the middle of the bottom (see Figure 1). The sides of the cube are 15 mm. The channel has two inlets, one horizontal channel flow with a *low* velocity and one vertical impinging jet with a *high* velocity. The impinging jet enters through a circular nozzle at the middle of the top plate. The cube consists of an isothermal core of 70ºC covered with an epoxy layer with low thermal conductivity and a thickness, δ_c, of 1.5 mm (see Figure 1). The geometrical and flow details and the material properties are summarized in Tables 1 and 2. The cooling medium is air.
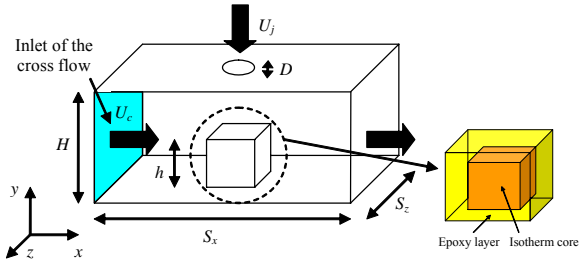

Figure 1. Computational domain.

The following boundary conditions are used: The top and bottom walls are adiabatic with no-slip conditions. Symmetric boundary conditions are used for the sidewalls and zero gradient condition for the outflow (i.e. $\partial U/\partial x = \partial T/\partial x = 0$) with a overall mass balance correction. The same temperatures of 20ºC will be used for the cross-flow and the impinging jet. The velocity profile and the turbulent properties at the inlet of the cross flow (see Figure 1) are predicted from a larger separate simulation with a row of wall-mounted cubes and the same geometrical configuration as in Figure 1 under a fully-developed channel flow. The boundary conditions for the impinging jet, that is the velocity profile, turbulent kinetic energy and turbulent dissipation rate is derived from the measurements by Tummers et al. [22]. A curve fit from the velocity measurements is used to define the velocity profile, *V*. The turbulent kinetic energy, $k = 0.5(\overline{u'^2} + \overline{v'^2} + \overline{w'^2})$, is calculated by assuming that the stream-wise and span-wise Reynolds stresses, $\overline{u'^2}$ and $\overline{w'^2}$, are identical and the values for $\overline{u'^2}$ and $\overline{v'^2}$ are obtained from the above mentioned measurements. The turbulent dissipation rate, ε, is estimated by

$$\varepsilon = C_\mu^{3/4} \frac{k^{3/2}}{l} \tag{1}$$

where C_μ is an empirical constant with a value of 0.09 and *l* is a length scale given by $l = 0.07D$. It is worth mentioning that the mean velocities of cross-flow, U_c, and the impinging jet, U_j, are 1.73 and 6.50 m/s, respectively.

Table 1. Geometrical and flow details

D	12 mm
h	15 mm
H	$2h$ = 30 mm
S_x, S_z	$4h$ = 60 mm
δ_c	$0.1h$ = 1.5 mm
Re_j	8217
Re_c	4725

Table 2. Material properties

	Air	Epoxy layer
c_p	1006.43	1668.5
ρ	1.225	1150.0
λ	0.0242	0.236
μ	$1.789 \cdot 10^{-5}$	-----

2.2 Governing equations

The steady-state three-dimensional incompressible continuity and Reynolds equations are given by

$$\frac{\partial U_i}{\partial x_i} = 0 \tag{3}$$

$$\frac{\partial (U_j U_i)}{\partial x_j} = -\frac{1}{\rho}\frac{\partial p}{\partial x_i} + \frac{\partial}{\partial x_j}\left(\nu \frac{\partial U_i}{\partial x_j} - \overline{u_i' u_j'}\right) \tag{4}$$

$$\frac{\partial (U_j T)}{\partial x_j} = \frac{\partial}{\partial x_j}\left(\alpha \frac{\partial T}{\partial x_j} - \overline{u_j' T'}\right) \tag{5}$$

where U_i is the mean velocity and u_i' is the fluctuating velocity. The $\overline{u_i' u_j'}$ and $-\overline{u_j' T'}$ are the modified Reynolds stresses and the modified turbulent heat fluxes and must be modelled in order to close the system equations. The modified turbulent heat fluxes, $-\overline{u_j' T'}$, are modelled by the eddy-diffusivity hypothesis with constant turbulent Prandtl number, Pr_t, as

$$-\overline{u_j' T'} = \frac{\nu_t}{Pr_t}\frac{\partial T}{\partial x_j} \tag{6}$$

Two turbulence models are investigated in this study, a $\overline{v^2}$-f model and a Reynolds stress model (RSM). The proposed model for the turbulent diffusion by Lien and Leschziner [14] is used in the RSM. The dissipation part in the RSM is modelled with the isotropic dissipation assumption and the pressure-strain term, Φ_{ij}, is modelled by a linear approach proposed by Launder and Shima [11]. The near-wall region in the RSM is completely resolved all the way through the viscous sub-layer by a two-layer approach. The two-layer model is based on the one-equation model of Wolfshtein [23], with use of the turbulent length scales proposed by Chen and Patel [2]. Details about the above-mentioned turbulence models can be found in the articles by Rundström and Moshfegh [20, 21] and in the Fluent Manuals [6]

2.3 Numerical details

The finite-volume code Fluent 6.2.16 was used to numerically solve the governing equations with a segregated scheme and the SIMPLE algorithm solved the pressure-velocity coupling, see Table 3.

Table 3. Numerical scheme

Grid	Staggered grid
Pressure-Velocity-Coupling algorithm	SIMPLE
Discretization schema	
Non-linear terms	Second-order upwind schema
Viscous terms	Second-order central scheme

The mesh consists of 881,832 structured hexahedral cells. There are 42×42 cells near the sidewalls of the cube. The top of the cube consists of a total of 5,876 cells. The circular inlet and the region under the impinging jet consist of 2,516 cells in the *xz*-

plane. The mesh is refined enough near the solid walls ($y^+ < 1$) to solve the all boundary layer with the two-layer model, see Figure 2. There are five cells with identical spacing through the epoxy layer and there are 64,660 cells located in the epoxy layer. A grid independency study was performed by Rundström and Moshfegh [19].
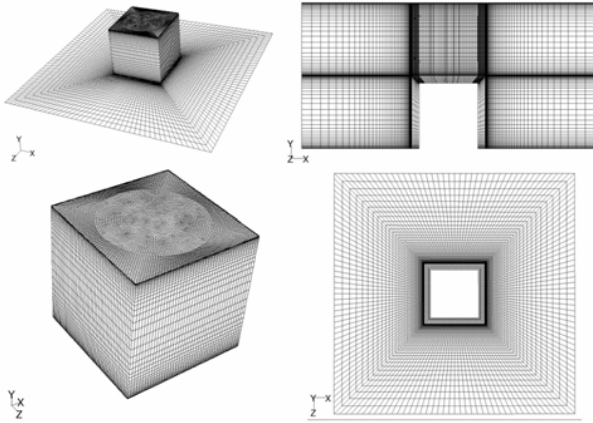

Figure 2. Computational grid for the case with $h = 15$ mm, perspective view (upper left), side view (upper right), cube surface (lower left), top view (lower right).

3. Experimental procedure

The numerical models described in section 2 are verified against particle image velocimetry (PIV) measurements for the velocity field and temperature measurements by use of an infrared imaging system.
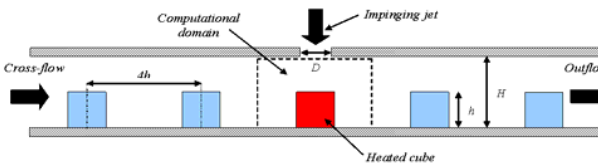
3.1 Experimental set-up

Figure 3. Schematic sketch of the experimental set-up.

The experimental set-up is shown in Figure 3. The experimental equipment consists of a wind tunnel with five cubes mounted in line in the middle of the tunnel; only the third is heated in the present study. The size of the cubes is 15 mm and the distance between each pair of cubes S_x is 60 mm. The tunnel has a height H of 30 mm and a width of 360 mm. One impinging jet is positioned above the third cube. The impinging jet is forced through a circular hole with a diameter, D, of 12 mm. The centres of the impinging jets and the third cube are identical. The impinging jet is provided with air from a separate channel placed above the top plate. All measurements are carried out at the third cube (see Figure 3).

3.2 Measurements

The time-average velocity field and the Reynolds components were measured in the xy and xz planes with a PIV system. The PIV system included a double-pulsed Nd:YAG laser with a pulse energy of 25 mJ. The laser was used to produce an approximately 1 mm light sheet that illuminated the seed particles in the flow. A PCO Sensicam camera recorded the images of the seed particles in the light sheet. For each plane, 1000 image pairs were acquired and the commercial software VidPIV Rowan v4.0 was used to analyse the images.

The time-averaged temperature distribution on the cube was measured by a low-wavelength (2 to 5.5 μm) infrared imaging system (Varioscan, Jenoptik). The Varioscan camera is equipped with a scanning mechanism to create images that are composed at 200 lines with 300 pixels. The relation between the pixel intensity and the temperature is established in an in-situ calibration procedure in conjunction with an image restoration technique based on a Wiener filter, using the two-dimensional optical transfer function as described by Meinders et al. [16]. These temperature and PIV measurements were carried out at the Department of Applied Physics, Delft University of Technology, Delft, the Netherlands, see Tummers et al. [22] for more details.

4. Results

4.1 Impinging jet in a Cross-flow

The velocity field from the models and the PIV measurements are illustrated by contour plots of the velocity magnitude in the xy-plane at the centre of the channel (see Figure 4). The path-lines from the simulation with the RSM are used to illustrate the three dimensional velocity structures (see Figure 5).
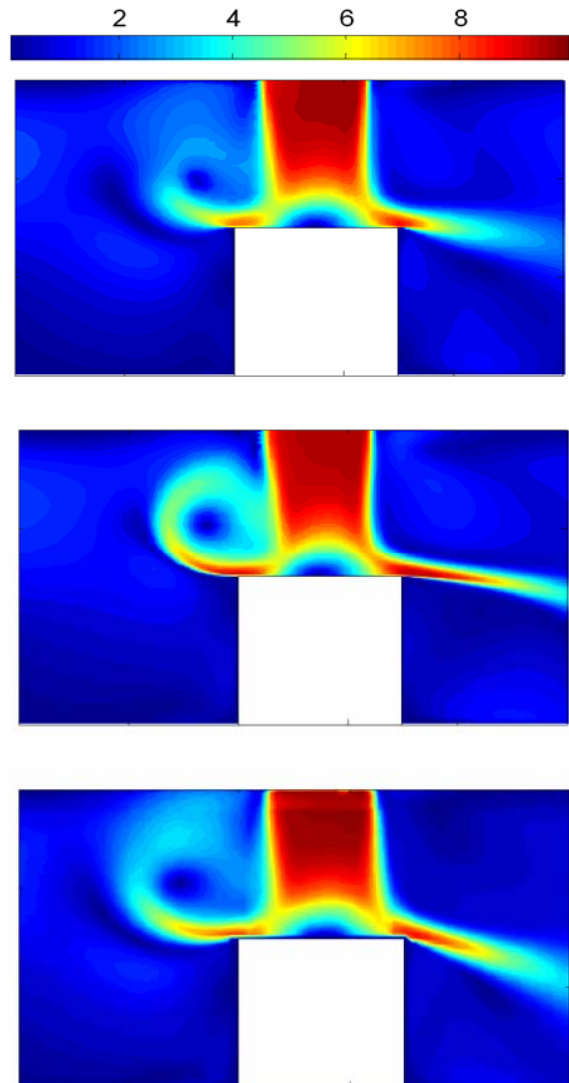

Figure 4. Contours of velocity magnitude, in the xy-plane, $z/h = 0$, RSM (upper), $\overline{v^2}$-f (middle) and PIV (lower).

The flow field shows a complex behaviour (see Figure 4 and 5) and there are several flow-related phenomena that can affect the cooling performance. For example, the position of the stagnation

318

point on top of the cube is an important factor for the prediction of heat transfer rate on top of the cube, and the separation from the top of the cube has an important effect on the heat transfer mechanisms at the other four walls.
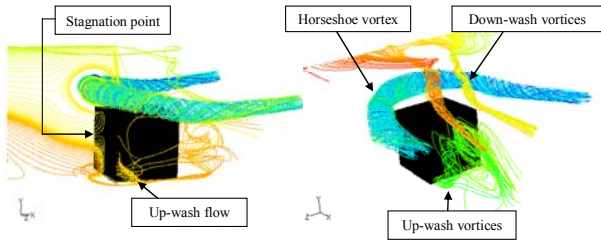

Figure 5. Path-lines from the simulation with the RSM.

The cross-flow has several flow-related effects on the impinging jet and the separation from the top of the cube. Figure 5 shows the characteristic horseshoe shape when the streamlines from the cross flow collide with the separated flow from the top of the front side, which results in a re-circulating vortex flow around the cube. A similar horseshoe vortex arises around the impinging jet (see Figure 5), which results in a deformation of the cross-section of the impinging jet and produces two re-circulating wake vortices and the counter-rotating vortex pairs (CVP). The impinging jet creates a downwash flow with a spiral-shaped feature due to the vortex pair.

The region behind the rear side of the cube consists of two vertical re-circulating vortices (perpendicular to the xz-plane) and one powerful horizontal vortex (perpendicular to the xy-plane) near the top of the cube (see Figures 4 and 5). These three vortices occur due to the separations from the sharp edges of the rear side. The vortices result in a spiral-shaped upwash flow near the rear side (see Figure 5).

The separation from the front side results in two small vertical vortices near each sidewall and the separated flow from the top create an up-wash flow near the sidewalls (see Figure 5). The up-wash flow is most significant near the reattachment points on the sidewalls, where the x-momentum is low and the separation from the top is most powerful.

The cross-flow in the lower part of the channel curls around the front face of the cube. The position of the stagnation point at the front side is located at approximately $y \approx 0.63h$. Figures 4 and 5 show that the cross-flow has been influenced by the two cubes downstream.

Figure 6 shows the normalized y-velocity component (V/U_j), $\overline{u'^2}$-Reynolds stress, $\overline{v'^2}$-Reynolds stress and turbulent kinetic energy, k, in the centre of the impinging jet as a function of the normalized vertical distance y/H.
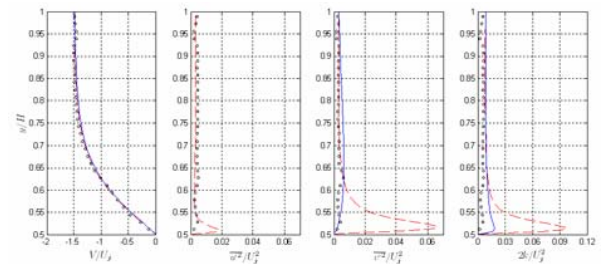

Figure 6. y-velocity component (V/U_j), $\overline{u'^2}$-Reynolds stress, $\overline{v'^2}$-Reynolds stress, turbulent kinetic energy, k, at $x/h = z/h$=0. — = $\overline{v^2}$-f, --- = RSM, o = PIV measurement.

The left diagram in Figure 6 shows that the y-velocity component is almost constant when $0.85 < y/H$, a rapid decreasing behaviour is observed between $0.85 \leq y/H \leq 0.55$ and a linearly decreasing behaviour when $y/H \leq 0.55$. The agreement between the PIV measurements and the simulations are good. The only deviation from the PIV measurements is in the region where V/U_j decreases sharply. The results from the simulations show somewhat lower values in the above-mentioned region.

The second diagram in Figure 6 shows that the values of the $\overline{u'^2}$-Reynolds stress is higher near the wall (i.e., when $y/H \leq 0.53$) in the RSM than in the PIV measurements and a significantly peak is observed in the RSM at $y/H \approx 0.51$. The $\overline{u'^2}$-Reynolds stress is almost constant from the outlet of the nozzle down to the distance of $y/H \leq 0.55$ where a rapid increase in $\overline{u'^2}$-Reynolds stress occurs in the RSM.

The third diagram in Figure 6 shows that the RSM predicts a much higher level of $\overline{v'^2}$ Reynolds stress in the stagnation region than the $\overline{v^2}$-f model and the PIV measurements do. The increase of $\overline{v'^2}$ Reynolds stress with increasing y-coordinates is much faster in the RSM near the wall (i.e., when $y/H = 0.5$) than in the $\overline{v^2}$-f model and the PIV measurements, and the maximum value is more than seven times larger in the RSM than in the PIV measurements and in the $\overline{v^2}$-f model. This is a well-known phenomenon for impinging flows when the modelling of the wall-reflection term in the pressure-strain term is based on the model by Gibson and Launder [8]. Craft et al. [4] observed similar results when this pressure-strain model was used.

The left diagram in Figure 6 shows that the RSM predicts a significantly higher level of the turbulent kinetic energy, k, is in the stagnation than the $\overline{v^2}$-f model and the PIV measurements. The turbulent kinetic energy from the PIV measurements has been estimated by assuming that the span-wise components are identical with the stream-wise components. A maximum value can be observed in for both the RSM and the $\overline{v^2}$-f model at $y/H \approx 0.51$ but the size of the maximum value is more than five times larger in the RSM than in the $\overline{v^2}$-f model.
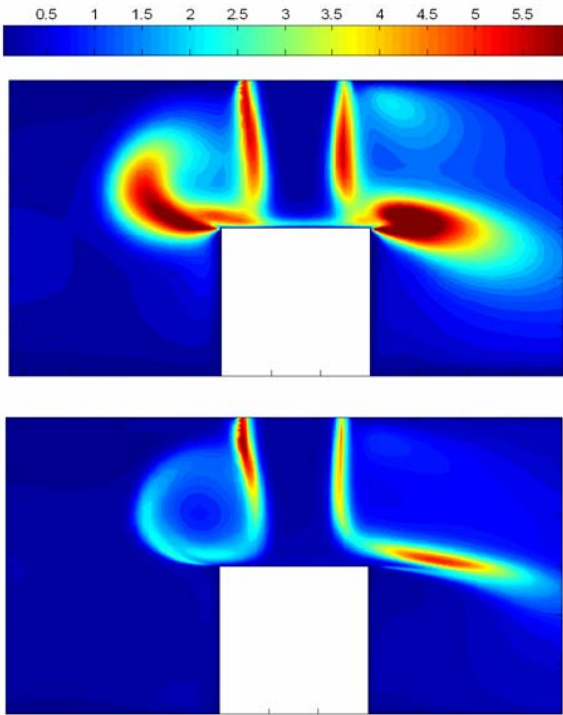
Figure 7. Contours turbulent kinetic energy, k, in the xy-plane, $z/h = 0$, RSM (upper), $\overline{v^2}$-f (middle) and PIV (lower).

The turbulent kinetic energy, k, is used to compare the turbulence characteristics between the two turbulence models. Figure 7 shows that the RSM predicts a significantly higher level of turbulent kinetic energy in the stagnation region than the $\overline{v^2}$-f model. The same trend can be observed at the separation from the top of the cube and in the free shear region between the impinging jet and the cross-flow. The RSM seems to have higher net production of k in the free shear regions (i.e. far from the walls) and is more diffusive than the $\overline{v^2}$-f model in these regions.

Figure 8 shows the normalized x-velocity component (U/U_j) as a function of the vertical distance (y/H) near the third cube. Each diagram represents different locations in the x-direction at the centre of the cube. The first diagram represents the line at the distance $0.75h$ downstream from the centre of the cube (i.e. $x/h = -0.75$), and the four following diagrams represent the following x-positions: $x/h = -0.25$, $x/h = 0.5$, $x/h = 0.75$, $x/h = 1$ and $x/h = 1.5$ where the last four x-positions represent the distance upstream
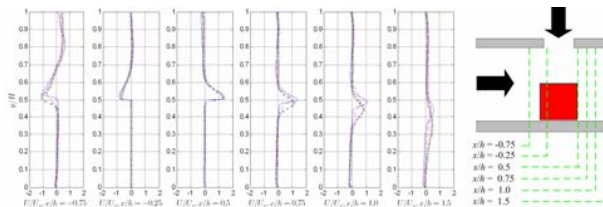

Figure 8. x-velocity components (U/U_j) in the xy-plane, $y/H = 2/15$.
—— = $\overline{v^2}$-f, --- = RSM, o = PIV measurement.

from the centre of the cube.

The second and third diagrams in Figure 8 show good agreement between the RSM, $\overline{v^2}$-f model and the PIV measurement in the stagnation region. Both models show good agreement with the PIV measurement in the recirculating region before the front side of the cube where the magnitudes of the peaks are somewhat

lower in the RSM than in the $\overline{v^2}$-f model (see the first diagram on the left in Figure 8). The agreement between PIV measurements and the $\overline{v^2}$-f model is somewhat better than between the RSM for the peak in the lower part of the recirculation region ($0.45 \leq y/H \leq 0.6$) at $x/h = -0.75$. The RSM and the PIV measurement show almost identical behaviour at the upper part of the recirculation region ($0.7 \leq y/H \leq 0.9$) at $x/h = -0.75$ where a stronger recirculation is observed in this region for the $\overline{v^2}$-f model. The strong separation from the rear side is also well predicted by the models where the results from both models are almost identical with the PIV measurements (see the third diagrams from the left in Figure 8) but the separated flow seems to be more forced against the bottom plate in the PIV measurement than in the simulations, which results in a lower position of the maximum value in the PIV measurement than in the RSM and in the $\overline{v^2}$-f model (see the three last diagrams in Figure 8). The predicted peaks from the RSM seems to decrease faster than the peaks in the $\overline{v^2}$-f model and in the PIV measurement and the maximum value of the peaks in this region are higher in the $\overline{v^2}$-f model than in the PIV measurements (see the three last diagrams in Figure 8).

Figure 9 shows the normalized x-velocity component (U/U_j) as a function of the spanwise distance (z/h) at the vertical location of 4 mm (or $y/H = 2/15$). Each diagram represents the same x-positions as in Figure 8.
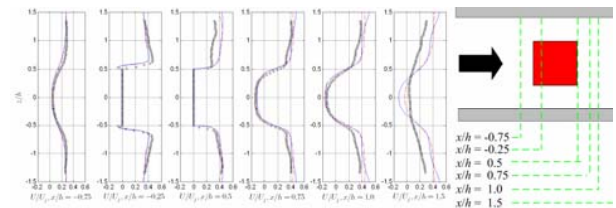

Figure 9. x-velocity components (U/U_j) in the xz-plane, $y/H = 2/15$.
—— = $\overline{v^2}$-f, --- = RSM, o = PIV measurement.

The blockage effect in front of the front side of the cube are good predicted by both models and are in very good agreement with the PIV measurement (see the first diagram in Figure 9). The bypass flow is in good agreement between the RSM, the $\overline{v^2}$-f model and the PIV measurement and the predictions of the separated flows from the sidewalls are also in good agreement with the PIV measurement (see the second and third diagrams in Figure 9). The agreement between the predictions and the PIV measurement in the wake region behind the rear side is better close to the rear side than farther downstream from the wall there the minimum value in the centre are significantly lower in the $\overline{v^2}$-f model than in the RSM and in the PIV measurements which indicates that the length of the wake is larger in the $\overline{v^2}$-f model than in the RSM and in the PIV measurements (see the last diagram in Figure 9). The agreement is better in both predictions near the centreline ($-0.5 \leq z/h \leq 0.5$) than in the periphery at $x/h = 0.75$ and $x/h = 1.0$ (see the fourth and fifth diagrams in Figure 9). The results from both models show less diffusivity in the wake region than the PIV measurement and the RSM shows somewhat lower diffusivity than the LES in this region (see the sixth diagram in Figure 9).

Table 4 shows the average values of the heat transfer coefficient on each side of the cube and the average value of the whole cube. The diagrams in Figure 10 show the temperature distribution along two path lines on the surface of the cube.

Table 4. Predicted average heat transfer coefficient on each side of the cube from the RSM, and the $\overline{v^2}$-f model.

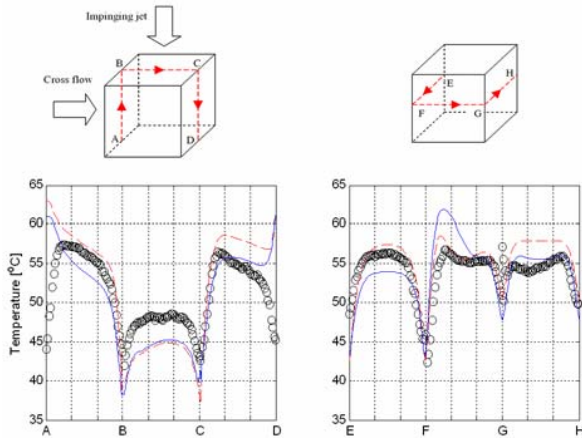|	Front	Top	Rear	Sides	Average
RSM	57.8	160.5	42.3	49.1	71.8
$\overline{v^2}$-f	90.4	137.3	58.9	46.5	75.9

Figure 10. Surface temperature, in the xy-plane, z/h = 0 (left), in the xz-plane, y/h = 0.5 (right). . —— = $\overline{v^2}$-f, —— = RSM, o = PIV measurement.

The results from the RSM and are in good agreement with the measurement on the front side of the cube where the results from the $\overline{v^2}$-f model are somewhat lower than in the RSM and in the measurement (see Figure 10). It can also be observed from Table 4 that the value of the average heat transfer coefficient on the front side of the cube is higher in the $\overline{v^2}$-f model than in the RSM. Both models predict approximately identical temperatures on the top of the cube. The heat transfer rate in the stagnation region seems to be a bit over-predicted by both models, due to the lower temperature on the top of the cube (see the left diagram in Figure 10). The value of the average heat transfer coefficient on the top of the cube is lower in the $\overline{v^2}$-f model than in the RSM (see Table 4). The predicted temperature from the RSM is higher than in both the $\overline{v^2}$-f model and in the measurements on the rear side of the cube. The position of the maximum value is located at approximately identical position in the vertical direction by the RSM where the position is located at somewhat lower position in the $\overline{v^2}$-f model (see the left diagram in Figure 10), despite the fact that the maximum values of the temperature seems to be somewhat over-predicted in the RSM and somewhat under-predicted in the $\overline{v^2}$-f model. The average value of the heat transfer coefficient on the rear side is also higher in the $\overline{v^2}$-f model than in the RSM. A minimum in the measured temperature and in the $\overline{v^2}$-f model can be observed in the span-wise direction on the rear side of the cube, where the RSM shows an almost constant temperature (see the right diagram in Figure 10). The rapidly decreasing temperature in the measurement near the bottom plate can be explained by the heat losses through the base plate at the bottom of the cube (see the left diagram in Figure 10). The predicted temperatures show an increasing trend near the bottom plate due to the adiabatic boundary condition on the bottom plate. The predicted temperatures from the RSM agree well with the measurement on the sidewall of the cube. A maximum value is observed for both models and measurement at the front part of the sidewall where the re-circulating occurs. The predicted maximum value from the $\overline{v^2}$-f model is much higher in than in the results from the RSM and the measurement. (see the right diagram in Figure 10). A significantly minimum value is

observed in the middle of the sidewalls in the RSM where the measurements shows an almost constant temperature and where the $\overline{v^2}$-f model shows a constant decreasing temperature along the path F-G. It can be noted that the re-attachment of the separations from the sidewalls occurs in this region i.e. at the rear part of the sidewalls Table 4 shows that the value of the average heat transfer coefficient on the sidewalls is somewhat lower in the $\overline{v^2}$-f model than in the RSM.

4.2 Impinging jet without cross-flow

There has not been a lot of work done on impinging flows in geometries other than flat plates. In this section, results from a jet impinging normally on a circular pedestal of height, h=D/1.06, and radius h/2 is presented. The pedestal is heated and mounted on a flat plate. Computed streamlines from this simulation is shown in Figure 11. The fluid emanating from the jet decelerates in the axial direction at the top of the pedestal. The flow then turns sharply and forms a radial wall jet along the upper surface of the pedestal. At the corner of the pedestal, the flow separates and reattaches downstream on the plate. This creates a recirculation region that has a significant effect on the wall heat transfer. This bubble is much shorter than that found downstream of a backward-facing step (recirculation lengths between 5 and 8 times the step height); the rather short length is due to the strong influence of the outer region of the impinging jet and the axisymmetric nature of the flow. After reattachment, the flow develops into a wall jet along the plate. The ambient fluid outside the jet is entrained into the core with a developing shear layer separating the core and the ambient fluid. This entrainment is illustrated by the curvature of the streamlines outside the pipe towards the symmetry axis and leads to a small recirculation zone in the vicinity of the exit pipe-wall. This feature and the presence of a secondary recirculation near the bottom of the pedestal indicate a sufficient grid resolution around the exit of the nozzle and next to the pedestal.
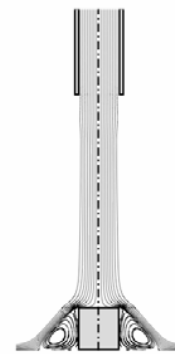

Figure 11. Flow on a pedestal

Figure 12 shows the local wall heat transfer distribution of an impinging jet on a wall-mounted pedestal. Simulations were carried out with the same parameters (Re=23,000 and H/D=6). Data from the numerical predictions are validated against the experimental data reported by Mesbah [5]. Similar to the flat plate simulations, predicted data obtained using the low-Reynolds-number k-ε model are not satisfactory. Figure 12 shows that the Launder and Sharma [10] k-ε prediction is more than 100% higher than the experimental values. Furthermore, the qualitative trend is also incorrect. Experimental data suggest that the spatial distribution of Nu in the stagnation region is a local minimum but the k-ε model predicts a local maximum. On the other hand, numerical predictions obtained using the V2F

321

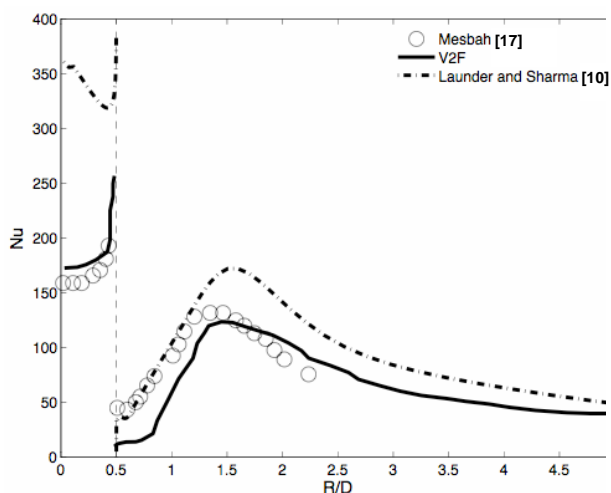turbulence model provide a good match with the experimental data, both qualitatively and quantitatively.

Figure 12. Radial distribution of the Nusselt number, Nu, on the top of the pedestal and on the bottom plate.

5. CONCLUSION AND DISCUSSION

The performance of a cooling technique with use of an impinging jet in a cross-flow on a heated wall-mounted cube was investigated numerically with use of a Reynolds stress model (RSM) and a $\overline{v^2}$-f model which has been verified for both the velocity and the surface temperature in the first part of this study. This case results in a very complex flow structure with several flow-related phenomena, such as stagnation points, separations, recirculation and curvature effects, which have influence on the heat transfer rate.

The results of the study has shown that both models predict the mean velocity field well in the stagnation region and in the other near-wall regions but the $\overline{v^2}$-f model seems to have more difficulties than the RSM to predict the turbulent diffusion in the free shear region (i.e. far from the walls) which results in an overpredicted size of the wake behind the cube. The RSM seems to predict the Reynolds stresses well in all regions except for the stagnation region above the cube where the $\overline{v'^2}$ Reynolds stress seems to be over-predicted. The main difference between the models is that the RSM produces a higher level of turbulent kinetic energy, k, than the $\overline{v^2}$-f model in all regions and the largest differences are in the stagnation region at the top of the cube. This lower turbulence intensity in the $\overline{v^2}$-f model seems to results in lower diffusivity in the free shear regions, which obviously can be observed in the separated flow from the top of the cube.

The predicted heat transfer rate from both turbulence models capture the main features on all five walls. The predicted heat transfer rate in the stagnation region on the top of the cube was higher in both models than in the measurements. The heat transfer rate in the stagnation region on the top of the cube is very sensitive to the boundary condition at the inlet of the impinging jet and the deviation between the predicted and measured temperatures on the top of the cube can partly be explained by the uncertainty of the boundary conditions at the inlet of the impinging jet and the relative simple model used for the turbulent heat fluxes (see equation 5)

References
[1] Brevet, P., Dejeu, C., Dorignac, E., Jolly, M. & Vullierme, J., Heat transfer to a row of impinging jets in consideration of optimization. *International Journal of Heat and Mass Transfer*, **45**, 2002, 4191–4200.
[2] Chen, H. C. and Patel, V. C., Near-wall turbulence models for complex flows including separation, *AIAA-Journal*, **26**, 1988, 641-648.
[3] Choi, M., Yoo, H., Yang, G., J.S. Lee, J. & Sohn, D., Measurements of impinging jet flow and heat transfer on a semi-circular concave surface. *International Journal of Heat and Mass Transfer*, **43**, 2000, 1811–1822.
[4] Craft, T. J., Graham, L. J. W. and Launder, B. E., Impinging jet studies for turbulence models. Assessment II: An examination of the performance of four turbulence models, *International Journal of Heat and Mass Transfer*, **36**, 1993, 2685-2697.
[5] Durbin, P., Near-wall turbulence closure modelling without damping function, *Theoretical and Computational Fluid Dynamics*, **3**, 1991, 1-13.
[6] Fluent 6.2., 2005, Fluent Manuals, Fluent Inc.
[7] Garimella, S. & Rice, R., Confined and submerged liquid jet impingement heat transfer. *Journal of Heat Transfer*, **117**, 1995, 871–877.
[8] Gibson, M. M. and Launder, B. E., Ground effects on pressure fluctuations in the atmospheric boundary layer, *Journal of Fluid Mechanics*, **86**, 1978, 491-511.
[9] Jonsson, H. and Moshfegh, B., Modeling of thermal and hydraulic performance of plate fin heat sinks – influence of bypass, *IEEE Transactions on Components and Packaging Technologies*, **24(2)**, 2001.
[10] Launder, B. E. and Sharma B. I., Application of the energy-dissipation model of turbulence to the calculation of flow near a spinning disc, *Letters in Heat and Mass Transfer*, **1**, 1974, 131-138.
[11] Launder, B. E. and Shima, N., Second-moment closure for near-wall sublayer: Development and application, *AIAA-Journal*, **27**, 1989, 1319-1325.
[12] Lee, J. & Baek, S., The effect of aspect ratio on the near-field turbulent structure of elliptic jets. *Flow Measurement and Instrumentation*, **5(3)**, 1994, 170–180.
[13] Lee, J. & Lee, S., The effect of nozzle aspect ratio on stagnation region heat transfer characteristics of elliptic impinging jet. *International Journal of Heat and Mass Transfer*, **43**, 2000, 555–575.
[14] Lien, F. S. and Leschziner, M. A., Assessment of turbulence transport models including non-linear RNG eddy-viscosity formulation and second moment closure for flow over a backward-facing step, *Computers and Fluids*, **23**, 1994, 983-1004.
[15] Meinders, E. R. and Hanjalić, Experimental study of the convective heat transfer from in-line and staggered configurations of two wall-mounted cubes, *International Journal of Heat and Fluid Flow*, **46**, 2002, 465-482.
[16] Meinders, E.R., van der Meer Th. H., and Hanjalić, K., September Application of infrared restoration technique to improve the accuracy of surface temperature measurements, *Proceedings of Quantitative Infrared Thermography 3*, EUROTHERM No. 50, 1996.
[17] Mesbah, M., An experimental study of local heat transfer to an impinging jet on non-flat surfaces: A cylindrical pedestal and a hemisphrically concave surface. *Ph. D. Thesis, University of California, Davis,* 1996.
[18] Obot, N., Mujumdar, A. & Douglas, A., Effect of semi-confinement on impinging heat transfer. *Proc. of the 7th Int. Heat Transfer Conf.,* 1982, 395–400.

[19] Rundström, D. and Moshfegh, B., Investigation of flow and heat transfer of an impinging jet in a cross-flow for cooling of a heated cube, *ASME-Journal of Electronic Packaging*, **128**, 2006, 150-156.

[20] Rundström, D. and Moshfegh, B., RSM predictions of an impinging jet in a cross flow on a wall-mounted cube, *Proceedings of the 13th International Heat Transfer Conference*, 2006.

[21] Rundström, D., and Moshfegh, B., RSM and $\overline{v^2}$-f study on the flow behaviour of an impinging jet in a cross-flow on a wall-mounted cube, *Progress in Computational Fluid Dynamics*, **7(2)**, 2007, 311-322.

[22] Tummers, M. J., Flikweert, M. A., Hanjalić, K., Rodink, R., Moshfegh, B., Impinging jet cooling of wall-mounted cubes, Proceedings of ERCOFTAC International *Symposium on Engineering Turbulence Modelling and Measurements - ETMM6*, 2005.

[23] Wolfshtein, M., The velocity and temperature distribution in one-dimensional flow with turbulence augmentation and pressure gradient, *International Journal of Heat and Mass Transfer*, **12**, 1969, 301-318.